JGR Oceans

RESEARCH ARTICLE
10.1029/2022JC019158

Key Points:

- The flume tests filled the data gap of relatively shallow-water waves interacting with opposing and following currents
- Two new modes of wave-current interaction effect on the excess pore pressure are identified in relation to the relative water depth
- An explicit solution for wave-current induced pore pressure is derived by incorporating the changes of both wave height and wavelength

Correspondence to:
W.-G. Qi,
qiwengang@imech.ac.cn

Citation:
Yang, L.-J., Qi, W.-G., Li, Y., & Gao, F.-P. (2023). Wave-current coupling effects on the variation modes of pore pressure response in a sandy seabed: Physical modeling and explicit approximations. *Journal of Geophysical Research: Oceans*, *128*, e2022JC019158. https://doi.org/10.1029/2022JC019158

Received 8 AUG 2022
Accepted 11 JAN 2023

Author Contributions:
Conceptualization: Wen-Gang Qi, Fu-Ping Gao
Data curation: Li-Jing Yang
Formal analysis: Li-Jing Yang, Wen-Gang Qi, Yuzhu Li
Funding acquisition: Wen-Gang Qi, Fu-Ping Gao
Investigation: Li-Jing Yang, Wen-Gang Qi
Methodology: Li-Jing Yang, Fu-Ping Gao
Project Administration: Wen-Gang Qi, Fu-Ping Gao
Supervision: Yuzhu Li, Fu-Ping Gao
Validation: Li-Jing Yang
Visualization: Li-Jing Yang, Wen-Gang Qi
Writing – original draft: Li-Jing Yang
Writing – review & editing: Wen-Gang Qi, Yuzhu Li, Fu-Ping Gao

Wave-Current Coupling Effects on the Variation Modes of Pore Pressure Response in a Sandy Seabed: Physical Modeling and Explicit Approximations

Li-Jing Yang[1,2], Wen-Gang Qi[1,2], Yuzhu Li[3], and Fu-Ping Gao[1,2]

[1]Institute of Mechanics, Chinese Academy of Sciences, Beijing, China, [2]School of Engineering Science, University of Chinese Academy of Sciences, Beijing, China, [3]Department of Civil and Environmental Engineering, National University of Singapore, Singapore, Singapore

Abstract Previous flume observations on the response of pore pressure in the seabed induced by the combined wave-current were mainly limited to relatively deep-water waves with wavenumber times water depth approximately above 1.0. Meanwhile, existing theoretical solutions neglected the variation of wave height induced by wave-current coupling effects, limiting the accuracy of the predictions. In this study, the combined wave-current induced pore pressure response within a sandy seabed is physically modeled in a water flume. A wide range of wave-current parameters is examined. The effects of wave period, water depth, and wave height with the superimposed following and opposing currents on the change of pore pressure are investigated. The present experiments identify two new particular modes of pore pressure changing under superimposed current on waves, that is, the transition mode and the opposing-current enhancing mode, besides the well-recognized following-current enhancing mode. The specific modes are determined by a dimensionless parameter characterizing the value of wavenumber times water depth for waves in the absence of a current. Based on the conservation of mass, momentum, and energy flux, an explicit solution for the wave height under the wave-current coupling effect is derived. With this updated wave height, an analytical solution for combined wave-current induced pore pressure response is further proposed, which agrees with the measured data. Based on this solution, a general diagram for the current effect on the mudline pore pressure amplitude is proposed, which is applicable for both laboratory and field conditions. Finally, the physical mechanism in three variation modes is discussed.

Plain Language Summary In the natural ocean environment, waves usually coexist with currents. The coexisting current can have significant influences on waves and the wave-induced pore pressure response in marine sediments. However, so far, there has not been any comprehensive study on pore pressure response in the sandy bed under combined waves and currents. To fill this gap, we performed a number of experiments in a large-scale flume to physically model pore pressure response in a sandy seabed under different combinations of waves and currents, considering wider conditions than existing laboratory studies. Then, an analytical solution for wave-current induced pore pressure was established. For modes of pore pressure variation with combined wave-current, in contrast to the previous well-accepted conclusion that only one mode exists, two other new modes are identified in the present study. The present physical investigation and theoretical analyses have for the first time established a general diagram for the wave-current coupling effect on the pore pressure, providing insightful information on the seabed response under natural loadings.

1. Introduction

In the natural near-shore environment, waves often coexist with currents, which can induce excess pore pressure in the porous marine sediments and weaken the stability of the seabed. The dynamic interaction of waves, currents, and the seabed has been considered critical in the studies of sediment transport and local scour (e.g., Anderson et al., 2017; Li, Ong, Fuhrman, & Larsen, 2020; Qi & Gao, 2014), seabed liquefaction (e.g., Klammler et al., 2021; Li, Ong, & Tang, 2020; Zhou, Liu, et al., 2021; Zhou, Qi, et al., 2021), and instability of offshore foundations (e.g., Cuéllar et al., 2012; De Groot et al., 2006; Oumeraci, 1994). Nevertheless, existing laboratory experiments for combined wave-current induced pore pressure have been limited to small wave periods, and most previous theoretical research did not consider the wave-current coupling effects adequately. Until today, a

comprehensive understanding of pore pressure response in the seabed induced by the combined wave-current is still lacking.

Numerous existing theoretical studies have been carried out to quantify the dynamic pore pressure response under wave-only conditions, with various assumptions under the framework of Biot's poroelastic theory (Biot, 1941). Among these, Yamamoto et al. (1978) proposed an analytical solution for the infinite and isotropic seabed with consideration of compressible pore fluid and soil skeleton. In the same year, a theoretical solution for hydraulically anisotropic seabed with infinite thickness was derived by Madsen (1978). The wave-induced pore pressure response has also been measured in both laboratory experiments (Chowdhury et al., 2006; Zhang et al., 2016) and field observations (Michallet et al., 2009; Zen & Yamazaki, 1991), which provide validations for the analytical solutions. Besides theoretical analyses and physical observations, numerical models were also employed to investigate wave-induced excess pore pressure for cases with complex boundary conditions (Chang & Jeng, 2014; Li, Ong, & Tang, 2020; Lin et al., 2016; Sui et al., 2016). Detailed reviews of previous investigations on wave-seabed interaction have been given in Jeng (2018).

All the above mentioned studies were limited to wave-only conditions. Nevertheless, the coexistence of waves and currents is a common phenomenon in natural coastal environments. The superimposed current could affect wave profiles significantly, especially in the shallow sea (Peregrine, 1976). As reviewed by Zhang et al. (2021), wave-current interaction has received extensive attention in the past decades. Longuet-Higgins and Stewart (1960, 1961) first proposed the concept of radiation stress to describe the coupling between waves and currents. Later, based on the conversation of mass, momentum, and energy flux, Whitham (1962) established governing equations for wave-current interaction. The studies of Longuet-Higgins and Stewart (1961) were discussed as special cases in Whitham (1962). Employing a similar approach to that of Whitham (1962), Baddour and Song (1990b) investigated the characteristics variations of the wave-current field after the interaction between linear waves and uniform currents. Nevertheless, their solutions were not explicit and needed to be calculated numerically. Their results indicated an increasing wavelength and decreasing wave height due to following currents, which were validated by the experimental results of Thomas (1981). A similar phenomenon was also observed in numerous other experimental studies (e.g., Brevik & Bjørn, 1979). Baddour and Song (1990a) further extended their studies to the second order waves.

The variation of wave parameters induced by coexisting currents can further affect the dynamic pore pressure in the seabed. Ye and Jeng (2012) made the first attempt to study the soil response under a wave and current loading with numerical simulations, although by simply considering the effects of current on wavelength. Based on Biot's poroelastic dynamic theory (u-p approximation), and applying the third-order approximation of nonlinear wave-current interaction (Hsu et al., 2009) as the boundary condition at the mudline, Ye and Jeng (2012) revealed that the difference of pore pressure between with and without a superimposed current can reach up to 25%. Adopting the same boundary condition, analytical solutions for the wave–current induced oscillatory soil response were proposed in Zhang et al. (2013), Liu et al. (2014), and Liao et al. (2015), considering quasi-static, partly dynamic, and fully dynamic soil behaviors, respectively. These numerical and analytical studies all indicated that superimposing a following current on existing waves will enhance the pore pressure response, while an opposing current will reduce it. This well-recognized relation will be named as "following-current enhancing mode" hereafter. Nevertheless, the current-induced variation of the wave height was inherently neglected in the above investigations, that is, the pre-interaction wave height was adopted to calculate the pressure loading at the mudline. The neglection of the change in wave height due to interaction with the current has a prominent influence on the dynamic loading (El-Shahat et al., 2021), as well as the pore pressure response (which shall be proved later in this work). Recently, Qi et al. (2019) conducted a series of flume tests on combined wave-current induced excess pore pressure in a sandy seabed. Although they have observed only the "following-current enhancing mode" (same as that in previous studies), they have also noticed that the effect of current gradually diminishes as the wave period increases. This seems to indicate that wave period can affect the wave-current interaction impact on pore pressure in the seabed. However, their flume tests have involved relatively deep-water waves (with wave period $T \leq 1.6$ s and water depth $h_0 = 0.5$ m, the water depth times wavenumber above 1.01), while the experimental data with waves with relatively shallow water depth are still lacking, as aforementioned.

To fill this gap, the present study performs a series of flume experiments to investigate the pore pressure response in a sandy seabed with a large range of wave periods. The water depth and wave height are also varied, with the bulk velocity of the currents approximately from −0.2 to 0.2 m/s. In order to establish a theory with proper

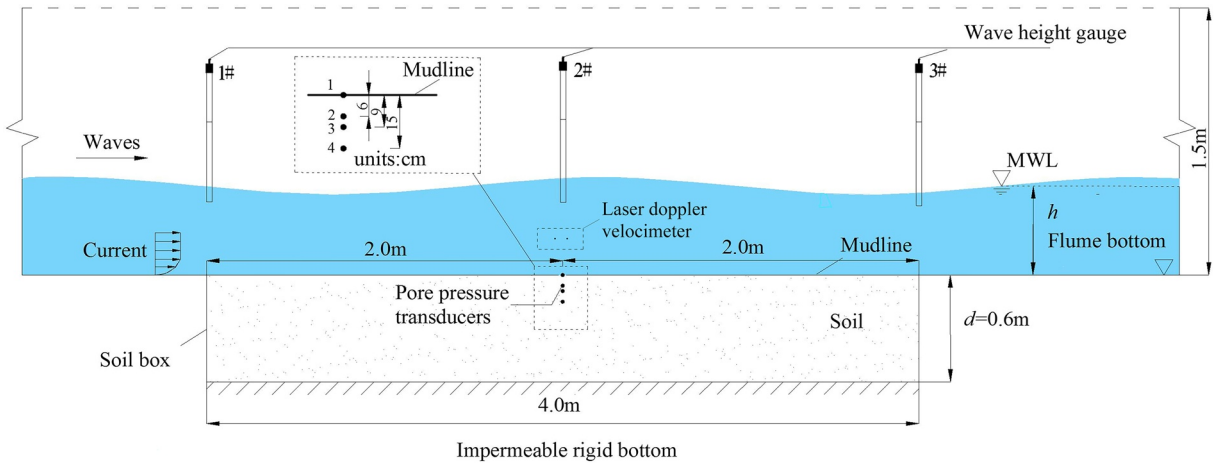

Figure 1. Schematic diagram of the physical modeling for combined wave-current induced excess pore pressure in a sandy bed, including flume and soil box profile and instrument locations.

consideration of the wave-current interaction, an explicit analytical solution of wave height after interacting with a uniform current is derived. The solution is further utilized to build a modified theory (from Zhang et al. (2013)) to predict the pore pressure response induced by combined waves and current in the poro-elastic sandy seabed. The remainder of the present paper is organized as follows: Section 2 describes the experimental set-up and test conditions. Results under different wave-current combinations are detailed in Section 3. Then, analytical solutions of wave height and pore pressure after wave-current interaction are theoretically derived and compared with the present experimental results for validation in Section 4. After that, parametric analyses for wave-current induced mudline pore pressure are conducted, with a general diagram for the wave-current coupling effect on the pore pressure given in Section 5. In addition, the physical mechanism in the experimental and theoretical results is discussed. Finally, Section 6 provides conclusions.

2. Experimental Study

2.1. Experimental Set-Up

The present physical modeling of combined wave-current induced pore pressure responses in a sandy seabed was performed in a large flume, which can concurrently generate periodic waves and a following or an opposing current. The major frame of the flume is 52.0 m in length, 1.0 m in width, and 1.5 m in depth. In the middle of the flume, a soil box of 4.0 m (length) × 0.6 m (depth) × 1.0 m (width) was constructed for preparing the sandy bed, as illustrated in Figure 1. A sandy seabed was prepared with a sand-raining device (Qi & Gao, 2014). The main physical properties of the sands are as follows: mean size of sand grains $d_{50} = 0.12$ mm, buoyant unit weight of soil $\gamma' = 9.70$ kN/m^3, relative density $D_r = 0.62$, coefficient of permeability $k_s = 9.60 \times 10^{-5}$ m/s, porosity $n = 0.40$, shear modulus $G = 10.0$ MPa, and the Poisson ratio $\nu = 0.30$.

As shown in Figure 1, four miniature pore pressure transducers (PPTs) were installed at different depths in the sandy bed to measure the pore pressure response. A Wave Height Gauge was located just above the PPTs. The other two WHGs were located above the upstream and downstream boundary of the sand bed, respectively, to calculate the wavelength according to the phase difference and the distance between the two WHGs. The signals of PPTs and WHGs were multichannel synchronously sampled by the data acquisition card with a sampling frequency of 100 Hz. A Laser Doppler Velocimeter (LDV) was utilized to monitor the flow velocity at a distance of 0.15 m to the flume bottom above the PPTs.

2.2. Experimental Procedure and Test Conditions

The general experimental procedures are similar to Qi et al. (2019), but with different details as follows: the PPTs for the present experiment were installed at 0, 6, 9, and 15 cm below the seabed surface, and the water depth of flume varied among 0.4/0.5/0.6 m. In addition, a LDV was used to monitor the flow velocity instead of the

Acoustic Doppler Current Profiler that was used in Qi et al. (2019). Different from the flume experiments limited to the relatively deep water depth in Qi et al. (2019), the present study investigates a wider range of wave-current parameters, and detailed information is given as follows.

The present test conditions for waves and currents are summarized in Table 1, where h_0 is the original water depth, H_0 is the measured wave height of wave-only conditions (i.e., pre-interaction wave height), H is the measured wave height in the wave-current field, T is the wave period, L is the measured wavelength in the wave-current field, and U_c is the measured current-only velocity (pre-interaction) at the level of 0.15 m above the sandy seabed. Based on the value of U_c, the mean bulk velocity of the current-only field (U_0) can be obtained from the logarithmic velocity distribution along the water depth (Qi et al., 2022). Current velocities between −0.2 and 0.2 m/s were considered. The present tests mainly consist of three series, aiming to reveal the effects of T (tests 1–45), h_0 (tests 46–75), and H_0 (tests 76–125) on the combined wave-current induced pore pressure response, respectively. A wide range of relative water depth kh from 0.58 to 3.07 was covered, where k and h are the wavenumber and water depth of the wave-current field, respectively. Note that all the present test conditions fall into the intermediate water depth range ($0.1\pi < kh < \pi$); therefore, the deep and shallow water in the present paper are relative within the intermediate water range. According to the diagram of the different wave theories application range (Le Méhauté, 1976), all the present test conditions fall into the Stokes 2nd/3rd order wave zones.

The sloping layered porous beach-type wave absorber at the end of the flume can reduce the wave reflection to below 5%. To further minimize the influence of wave reflection, the initial 10 stable wave cycles were utilized for data analysis. From the observed data, the best fitting curve in Stokes 3rd order wave theory ($P_b = A\cos\theta + B\cos 2\theta + C\cos 3\theta$) with minimum residual squares was back-calculated. To reflect the uncertainty of the observations, the coefficient of determination $R^2\left(=1-\frac{SS_{res}}{SS_{tot}}\right)$ (where SS_{res} is the sum of squares of residuals, SS_{tot} is the total sum of squares) of the mudline pore pressure data for each condition is given in Table 1. For most conditions, the coefficient of determination R^2 is generally above 0.99, proving the good stability of the experimental data. R^2 decreases to 0.943 only for Test 1 ($T = 1.0$ s, $h_0 = 0.6$ m, $H_0 = 8.47$ cm, $U_0 = -0.19$ m/s). Under this condition, the wave-only steepness H/L is large, and the superimposed opposing current further amplifies the wave steepness, causing the wave approaching the breaking condition and enlarging the uncertainty of the observation. For other conditions, R^2 remains close to or above 0.99. The uncertainty fluctuations brought by the superimposed following or opposing current are insignificant.

3. Experimental Results and Discussions

During all the tests, there was only oscillatory pore pressure but no residual pore pressure was observed due to the relatively large permeability coefficient of the soil. Under periodic waves, non-cohesive sediments are most prone to the instantaneous (momentary) liquefaction under the upward seepage induced by wave troughs (see Bear, 1972). Therefore, in the following analyses, the pore pressure amplitude specifically refers to that under wave troughs, which is a critical concern for evaluating seabed stability.

3.1. With Various Wave Periods

With three selected wave periods, the effect of current velocities on the distributions of pore pressure amplitude (P/P_{w0}, P_{w0} is the mudline pore pressure amplitude with wave-only conditions) along the soil depth is demonstrated in Figure 2. Three typical variation modes are identified from the experimental data as shown in Figure 2. In addition to that has been observed in previous studies (e.g., Qi et al., 2019), two new modes appear under relatively shallow-water conditions of laboratory tests. Each mode is detailed as follows:

1. Following-current enhancing mode: This mode is widely identified at the condition when the wave period is relatively small (Figure 2a with $T = 1.0$ s). In this mode, the superimposed following current ($U_0 > 0$) enlarges the pore pressure amplitude in the sandy seabed, whereas the opposing current ($U_0 < 0$) reduces it. In the present cases, the enhancing effect caused by the following-current is less prominent than the weakening effect induced by the opposing current. It is also seen that the following current increases the upward directed excess pore pressure gradient in the seabed near the mudline, which can raise the risk of instantaneous liquefaction and scour (Qi & Gao, 2014). This mode observed in the present study is consistent with that in Qi et al. (2019).
2. Opposing-current enhancing mode: In contrast to that with short-period waves, for relatively long-period waves in laboratory conditions (Figure 2b, $T = 2.4$ s), the superimposition with a following current causes

Table 1
Test Conditions for Wave-Current Induced Pore Pressure in a Sandy Bed

Test series	Test number	h_0 (m)	H_0 (cm)	T (s)	U_c (m/s)	U_0 (m/s)	L (m)	H (cm)	k_0h_0	R^2
Various wave period	1	0.6	8.47	1.0	−0.19	−0.20	1.23	10.70	3.07	0.943
	2				−0.10	−0.11	1.40	9.27	2.70	0.986
	3				0	0	1.54	8.47	2.45	0.984
	4				0.10	0.10	1.71	7.76	2.21	0.998
	5				0.20	0.21	1.86	6.87	2.03	0.988
	6		8.85	1.2	−0.19	−0.20	1.71	10.10	2.20	0.979
	7				−0.09	−0.10	1.94	9.67	1.95	0.997
	8				0	0	2.16	8.85	1.74	0.998
	9				0.10	0.10	2.31	8.10	1.63	0.995
	10				0.19	0.20	2.47	7.39	1.52	0.981
	11		8.31	1.4	−0.19	−0.20	2.28	9.73	1.65	0.998
	12				−0.10	−0.10	2.50	8.91	1.51	0.997
	13				0	0	2.67	8.31	1.41	0.998
	14				0.10	0.10	2.89	7.69	1.31	0.998
	15				0.19	0.20	3.08	7.28	1.23	0.998
	16		7.62	1.6	−0.20	−0.20	2.84	8.60	1.33	0.996
	17				−0.10	−0.11	3.02	7.98	1.25	0.998
	18				0	0	3.28	7.62	1.15	0.998
	19				0.10	0.10	3.48	6.96	1.08	0.996
	20				0.19	0.20	3.66	6.58	1.03	0.998
	21		8.25	1.8	−0.19	−0.20	3.40	9.33	1.11	0.996
	22				−0.10	−0.10	3.56	8.76	1.06	0.996
	23				0	0	3.77	8.25	1.00	0.997
	24				0.10	0.11	4.00	7.87	0.94	0.998
	25				0.19	0.20	4.16	7.59	0.91	0.998
	26		9.01	2.0	−0.20	−0.21	3.90	9.87	0.97	0.996
	27				−0.10	−0.11	4.10	9.38	0.92	0.997
	28				0	0	4.30	9.01	0.88	0.998
	29				0.10	0.11	4.60	8.68	0.82	0.997
	30				0.20	0.20	4.79	8.24	0.79	0.998
	31		9.29	2.2	−0.19	−0.19	4.40	10.26	0.86	0.996
	32				−0.10	−0.10	4.68	9.66	0.81	0.998
	33				0	0	4.89	9.29	0.77	0.997
	34				0.10	0.10	5.12	8.92	0.74	0.997
	35				0.20	0.21	5.37	8.58	0.70	0.998
	36		9.25	2.4	−0.20	−0.20	4.92	9.99	0.77	0.997
	37				−0.10	−0.10	5.22	9.63	0.72	0.998
	38				0	0	5.45	9.25	0.69	0.998
	39				0.10	0.10	5.63	8.89	0.67	0.997
	40				0.19	0.20	5.85	8.45	0.64	0.995
	41		8.95	2.6	−0.19	−0.20	5.45	9.65	0.69	0.995
	42				−0.11	−0.11	5.56	9.26	0.68	0.997
	43				0	0	5.78	8.95	0.65	0.997

Table 1
Continued

Test series	Test number	h_0 (m)	H_0 (cm)	T (s)	U_c (m/s)	U_0 (m/s)	L (m)	H (cm)	k_0h_0	R^2
	44				0.10	0.10	6.05	8.67	0.62	0.999
	45				0.19	0.20	6.30	8.22	0.60	0.996
Various water depth	46	0.4	8.45	1.2	−0.20	−0.20	1.60	9.69	1.57	0.996
	47				−0.11	−0.11	1.77	9.03	1.42	0.996
	48				0	0	1.94	8.45	1.30	0.998
	49				0.11	0.11	2.11	7.64	1.19	0.999
	50				0.20	0.20	2.26	7.23	1.11	0.999
	51	0.5	8.63		−0.20	−0.20	1.68	10.16	1.87	0.998
	52				−0.10	−0.10	1.90	9.18	1.65	0.997
	53				0	0	2.08	8.63	1.51	0.998
	54				0.11	0.11	2.25	7.76	1.39	0.998
	55				0.20	0.20	2.40	7.27	1.31	0.999
	56	0.6	8.85		−0.19	−0.20	1.71	10.10	2.20	0.979
	57				−0.09	−0.10	1.94	9.67	1.95	0.997
	58				0	0	2.16	8.85	1.74	0.998
	59				0.10	0.10	2.31	8.10	1.63	0.995
	60				0.19	0.20	2.47	7.39	1.52	0.981
	61	0.4	7.18	1.6	−0.20	−0.20	2.45	8.22	1.02	0.997
	62				−0.11	−0.11	2.66	7.59	0.95	0.999
	63				0	0	2.90	7.18	0.87	0.999
	64				0.11	0.11	3.03	6.73	0.83	0.997
	65				0.20	0.20	3.19	6.34	0.79	0.997
	66	0.5	7.32		−0.21	−0.21	2.68	8.19	1.17	0.996
	67				−0.09	−0.09	2.93	7.63	1.07	0.997
	68				0	0	3.10	7.32	1.01	0.999
	69				0.10	0.10	3.31	6.81	0.95	0.999
	70				0.20	0.20	3.46	6.24	0.91	0.999
	71	0.6	7.62		−0.20	−0.20	2.84	8.60	1.33	0.996
	72				−0.10	−0.11	3.02	7.98	1.25	0.998
	73				0	0	3.28	7.62	1.15	0.998
	74				0.10	0.10	3.48	6.96	1.08	0.996
	75				0.19	0.20	3.66	6.58	1.03	0.998
Various wave height	76	0.5	3.39	1.2	−0.20	−0.20	1.69	4.10	1.86	0.998
	77				−0.09	−0.09	1.90	3.73	1.66	0.999
	78				0	0	2.05	3.39	1.53	0.998
	79				0.10	0.10	2.22	3.11	1.41	0.999
	80				0.20	0.20	2.40	2.87	1.31	0.999
	81		5.16		−0.20	−0.21	1.71	6.28	1.83	0.999
	82				−0.10	−0.10	1.90	5.67	1.65	0.998
	83				0	0	2.08	5.16	1.51	0.999
	84				0.10	0.10	2.24	4.81	1.40	0.999
	85				0.20	0.20	2.42	4.35	1.30	0.999

Table 1
Continued

Test series	Test number	h_0 (m)	H_0 (cm)	T (s)	U_c (m/s)	U_0 (m/s)	L (m)	H (cm)	k_0h_0	R^2
	86		7		−0.19	−0.20	1.72	8.12	1.82	0.998
	87				−0.09	−0.09	1.90	7.55	1.65	0.998
	88				0	0	2.06	7.00	1.52	0.998
	89				0.09	0.09	2.22	6.38	1.42	0.999
	90				0.20	0.21	2.39	5.80	1.31	0.998
	91		8.63		−0.20	−0.20	1.68	10.16	1.87	0.998
	92				−0.10	−0.10	1.90	9.18	1.65	0.997
	93				0	0	2.08	8.63	1.51	0.998
	94				0.11	0.11	2.25	7.76	1.39	0.998
	95				0.20	0.20	2.40	7.27	1.31	0.999
	96		10.45		−0.20	−0.20	1.73	12.18	1.82	0.997
	97				−0.10	−0.10	1.90	11.37	1.65	1
	98				0	0	2.08	10.45	1.51	0.998
	99				0.09	0.10	2.23	9.44	1.41	0.999
	100				0.20	0.21	2.40	8.62	1.31	0.999
	101		3.42	2.4	−0.19	−0.20	4.44	3.77	0.71	0.995
	102				−0.09	−0.10	4.55	3.59	0.69	1
	103				0	0	4.85	3.42	0.65	0.999
	104				0.10	0.10	5.05	3.28	0.62	0.997
	105				0.20	0.20	5.20	3.19	0.60	0.998
	106		5.38		−0.20	−0.21	4.38	5.96	0.72	0.998
	107				−0.10	−0.10	4.65	5.67	0.67	0.999
	108				0	0	4.94	5.38	0.64	0.999
	109				0.10	0.10	5.11	5.26	0.62	0.999
	110				0.20	0.20	5.33	4.97	0.59	0.999
	111		7.41		−0.20	−0.20	4.44	8.25	0.71	0.998
	112				−0.09	−0.09	4.79	7.78	0.66	0.998
	113				0	0	4.97	7.41	0.63	0.999
	114				0.09	0.09	5.19	7.15	0.61	0.998
	115				0.20	0.20	5.37	6.89	0.58	0.998
	116		9.42		−0.20	−0.21	4.47	10.36	0.70	0.999
	117				−0.09	−0.09	4.69	9.78	0.67	0.999
	118				0	0	5.11	9.42	0.62	0.999
	119				0.10	0.10	5.25	9.03	0.60	0.998
	120				0.19	0.20	5.39	8.82	0.58	0.998
	121		11.3		−0.21	−0.21	4.49	12.40	0.70	0.999
	122				−0.09	−0.09	4.82	12.00	0.65	0.999
	123				0	0	5.09	11.30	0.62	0.998
	124				0.10	0.10	5.33	10.86	0.59	0.998
	125				0.20	0.21	5.46	10.47	0.58	0.998

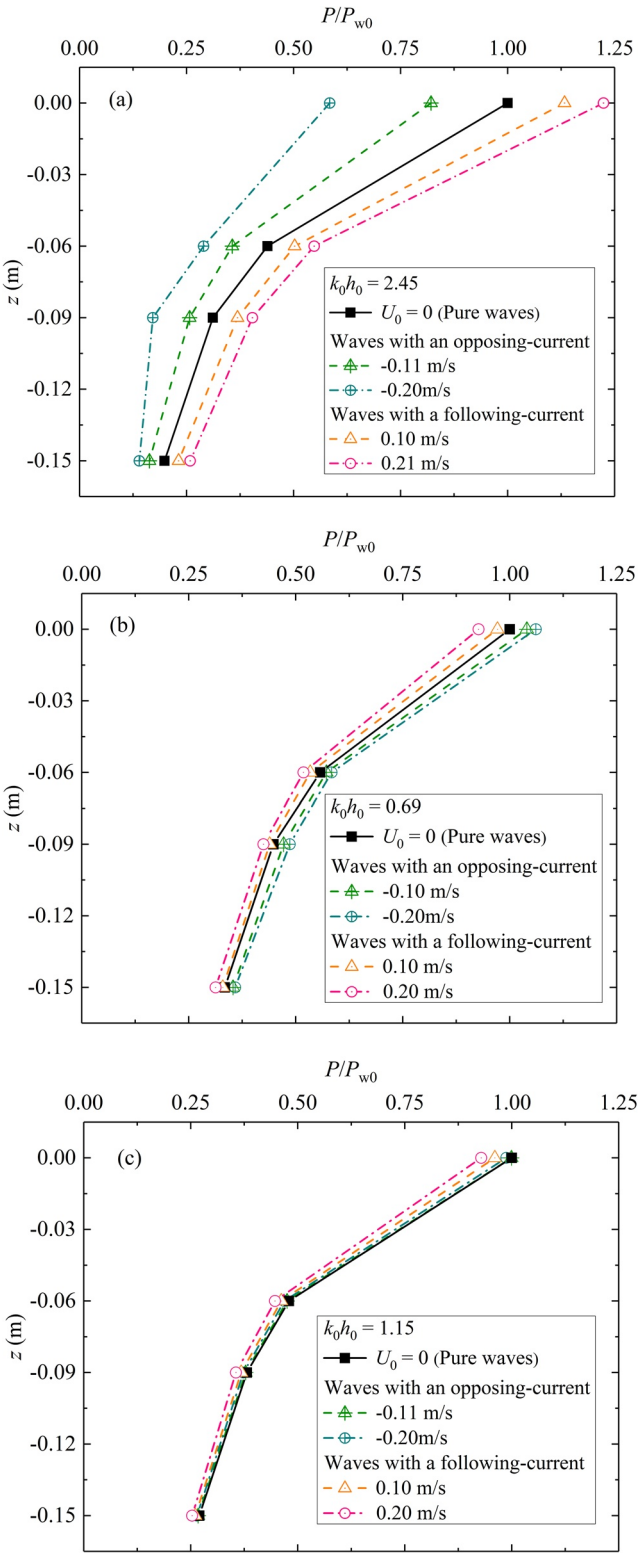

Figure 2. Effects of following/opposing currents with various velocities on the vertical distribution of pore pressure amplitude under different wave periods. For each case, the water depth and wave height generally keep constant, as shown in Table 1 ($H_0 = 8.44 \pm 0.82$ cm, $h_0 = 0.6$ m): (a) $T = 1.0$ s; (b) $T = 2.4$ s; (c) $T = 1.6$ s.

the excess pore pressure amplitude and gradient in the sandy seabed to decrease, while an opposing current enlarges them. In this mode, a following current can mitigate the seabed liquefaction risk, whereas the opposing current would pose more threats on the seabed stability. To the authors' best knowledge, this opposing-current enhancing mode has not been reported in previous investigations.

3. Transition mode: For intermediate-period waves in laboratory conditions (Figure 2c, $T = 1.6$ s), either following or opposing currents can reduce the excess pore pressure amplitude and gradient in the seabed. In this scenario, currents at a relatively large speed would always alleviate the risk of seabed instability, although the effect seems to be minor for the present cases.

Figure 3 further presents each curve in Figure 2 normalized by their own mudline pore pressure amplitude P_0 (under combined wave and current). It can be seen that the profiles generally coincide at each fixed wave period. This implies that the change of pore pressure is uniform along the depth due to the superimposition of a current. Therefore, we will focus on the mudline pore pressure amplitude P_0 in the following analyses.

To further present an overall picture of the three modes, Figure 4 shows the mudline pore pressure amplitudes under 5 typical current velocities with wave period increasing from 1.0 to 2.6 s at an interval of 0.2 s successively. Note that P_0 is non-dimensionalized by $\gamma_w H_0$ to eliminate the influence of various pre-interaction wave heights (H_0). The horizontal coordinate k_0h_0 is the relative water depth with wave-only conditions (k_0 denotes wavenumber in the wave-only field). Based on our preliminary tests and analysis, k_0h_0 is found to be a key parameter to determine the mudline pore pressure response (further discussions will be presented in Section 5). The filled circles in Figure 4 with the same color from light to dark represent the current velocity decreasing from 0.2 to −0.2 m/s under a certain wave period. The aforementioned three kinds of typical variation modes regarding the influence of a current can be clearly observed in this figure. In general, the range of $k_0h_0 > 1.4$, $1.1 < k_0h_0 < 1.4$, and $k_0h_0 < 1.1$ can be categorized as the following-current enhancing mode, transition mode, and opposing-current enhancing mode, respectively.

The three typical modes imply the inherent complexity of the current-induced variation of the pore pressure response in the seabed, which should be attributed to the nonlinear wave-current interaction. More information on this respect will be elaborated in Sections 4 and 5.

3.2. With Various Water Depths

Under the precondition of fixed values of wave period ($T = 1.2$ and 1.6 s) and wave height ($H_0 = 8.0 \pm 0.9$ cm), the effect of a current on the pore pressure amplitude under various water depths is also investigated in the present study. Note that the different values of k_0h_0 herein are due to the change of water depth (while in Figure 4 are because of varying wave periods). The effect of currents on the mudline pore pressure amplitude under various water depths is demonstrated by a series of symbols in Figure 5. Again, three typical variation modes can be observed. Moreover, the range of k_0h_0 for each mode is generally consistent with that in Figure 4 (by varying wave periods). This indicates that T and h_0 are not independent variables, confirming our preliminary identification of relative water depth k_0h_0 as the parameter to determine the variation modes. Note that this range of k_0h_0 is based on the present

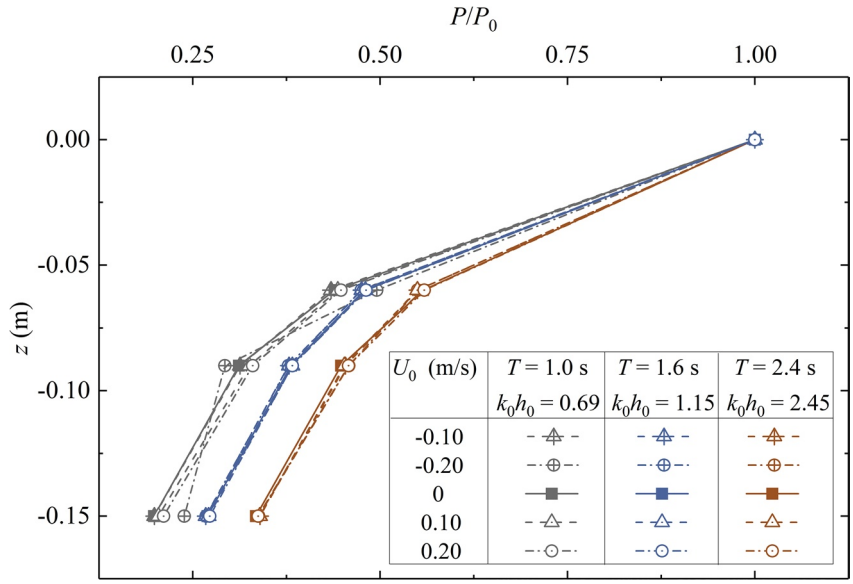

Figure 3. Comparison of the pore pressure amplitude attenuation along the soil depth normalized by corresponding mudline amplitude under different wave periods and current velocities ($H_0 = 8.44 \pm 0.82$ cm, $h_0 = 0.6$ m).

laboratory test conditions. The applicability of this conclusion, especially for field conditions, will be further verified with theoretical analyses in Section 5.

3.3. With Various Wave Heights

For two selected wave periods ($T = 1.2$ and 2.4 s), the effect of superimposed current on the mudline pore pressure under various wave heights is examined. As indicated by the pink lines and dots in Figure 6, waves with $T = 1.2$ s and $h_0 = 0.5$ m ($k_0h_0 = 1.51$) match the following-current enhancing mode, and the effect of the following/opposing current on P_0 is more or less the same for various values of H_0. In contrast, waves with a relatively shallow water depth ($T = 2.4$ s, $h_0 = 0.5$ m, $k_0h_0 = 0.63$), represented by the blue lines and dots in Figure 6, match the opposing-current enhancing mode, which is consistent with the previous discussion in Section 3.1. In addition, the effect of the current on P_0 is reinforced with increasing H_0, especially for the cases with a following current.

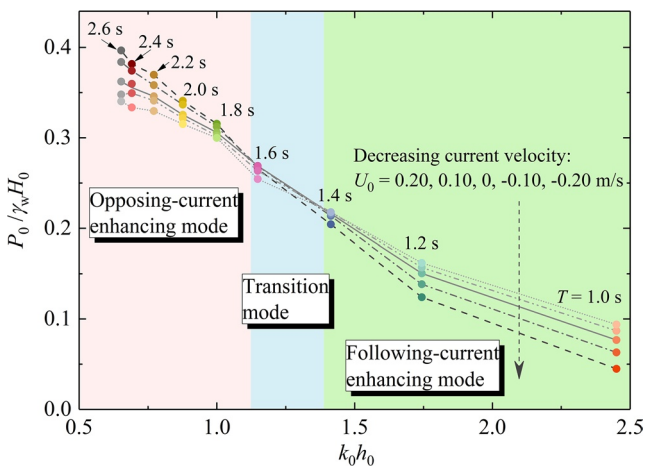

Figure 4. The observed variation of the mudline pore pressure amplitude with the superimposed current with different wave periods ($H_0 = 8.45 \pm 0.84$ cm, $h_0 = 0.6$ m, T varies between 1.0 and 2.6 s, see series 1 in Table 1 for more detailed parameters). Symbols and lines from light to dark within each color represent the current velocity decreasing from 0.2 to −0.2 m/s.

To further clarify the effect of wave height, Figure 7 gives the peak-to-peak values of mudline pore pressure P_p induced by combined wave-current with different wave heights. In contrast to the negative peak amplitude under wave trough P_0/P_{w0} (see Figure 6), P_p/P_{wp} (where P_{wp} is the peak-to-peak value for wave-only conditions) generally keeps constant with various H_0, for both relatively deep-water ($T = 1.2$ s, $k_0h_0 = 1.51$) and shallow-water waves ($T = 2.4$ s, $k_0h_0 = 0.63$), respectively.

According to the Stokes and cnoidal wave theories (Whitham, 1999), as the wave nonlinearity increases, the wave trough gets flattened. Therefore, the mudline pore pressure amplitude at wave trough of nonlinear waves decreases compared to that in linear waves. Figure 8 gives the ratios of P_0/P_p under different wave and current combinations. For cases with $T = 1.2$ s, the values of P_0/P_p with various current velocities and wave heights keep around 0.5, implying the dominance of linearity with symmetrical wave crest and trough. In contrast, for cases with $T = 2.4$ s, the ratio of P_0/P_p becomes less and less than 0.5 with increasing wave height, which is attributed to the asymmetry between wave trough and wave crest for highly nonlinear waves.

As afore-indicated in Figure 7, the effect of the superimposed current on the mudline pore pressure (characterized by P_p) is nearly irrelevant to the wave

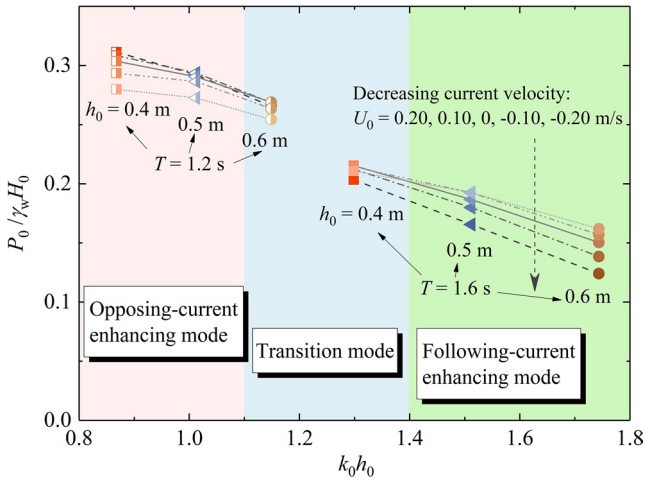

Figure 5. The observed variation of the mudline pore pressure amplitude with the superimposed current under different water depths ($H_0 = 8.02 \pm 0.84$ cm, $T = 1.2$ s/1.6 s, h_0 varies in 0.4/0.5/0.6 m, see series 2 in Table 1 for more detailed parameters). Symbols and lines from light to dark within each color represent the current velocity decreasing from 0.2 to −0.2 m/s.

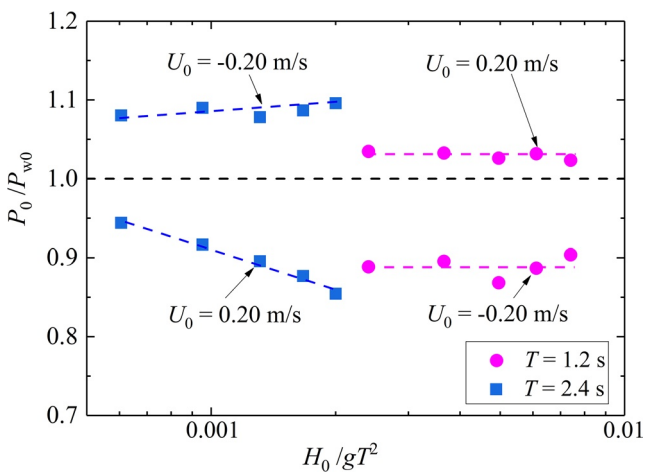

Figure 6. The variation of the mudline pore pressure trough amplitude against the normalized pre-interaction wave height for two typical wave periods with two current velocities ($h_0 = 0.5$ m). The result for wave-only conditions represented by the black dash line ($P_0/P_{w0} = 1$) is included for reference.

height. Therefore, for perfect linear waves with symmetrical crest and trough, the effect of current on P_0 is naturally independent on the wave height, as indicated by the pink circles in Figure 8. However, for small relative water depth with pronounced nonlinearity, the superimposed current would influence the asymmetry between wave crest and trough (see cases with $T = 2.4$ s in Figure 8). The effect of current on the wave asymmetry becomes more pronounced with increasing wave height, leading to the observed stronger influence of current on P_0. Note that this wave nonlinearity effect seems to be more obvious for the following current cases (i.e., $U_0 = 0.2$ m/s) compared with the opposing current cases (i.e., $U_0 = -0.2$ m/s), shown in Figures 6 and 8 with $T = 2.4$ s. The reason still needs to be further explored. It should be emphasized that the increase of wave height only amplifies the effect of the current on P_0, but does not change the variation mode.

4. Theoretical Derivation and Validation

In this section, the explicit solutions of wave height and pore pressure response in the wave-current field are derived. The solutions are further validated against the present experimental data and compared with the previous analytical solutions of Zhang et al. (2013). A wave-current interaction approach similar to Baddour and Song (1990b, 1990a) and Whitham (1962) is adopted to construct the present analytical model, on the basis of the conservation of mass, momentum, and energy flux. Defining the mean level of the water surface as $z = 0$, the schematic of the model is shown in Figure 9, where η_0 is the wave-only surface elevation, a_0 is the wave-only (pre-interaction) amplitude, L_0 is the wave-only length, η is the wave-current surface elevation, a is the wave amplitude after wave-current interaction, and U is the average velocity of the wave-current field. Note that to make the theoretical analysis possible, the current was assumed to be depth-uniform with mean bulk velocity U_0.

4.1. Expressions of Mass, Momentum, and Energy Flux

The expressions of mean mass Q, momentum M, and energy flux E over a wave period across a fixed vertical surface are provided in this section, with the subscript w, c, and wc indicating the condition of wave-only, current-only, and wave plus current, respectively. For a two-dimensional flow in the wave-only field (Whitham, 1962):

$$Q_w = \overline{\int_{-h_0}^{\eta_0} \rho u_0 dz}, M_w = \overline{\int_{-h_0}^{\eta_0} (P_w + \rho u_0^2) dz},$$

$$E_w = \overline{\int_{-h_0}^{\eta_0} \left[P_w + \frac{\rho}{2}(u_0^2 + w_0^2) + \rho g(z + h_0)\right] u_0 dz} \quad (1)$$

where the overbar denotes the mean value over a wave period, ρ is the fluid density, g is the gravitational acceleration, P_w is the pressure of the wave-only field, u_0 and w_0 are the horizontal and vertical velocity component of the wave-only field, respectively. In the current-only field with depth-uniform velocity, the expressions are written as:

$$Q_c = \rho h_0 U_0, M_c = (Q_w + Q_c) U_0,$$

$$E_c = \frac{1}{2}(Q_w + Q_c) U_0^2 + \int_{-h_0}^{0} [P_c + \rho g(z + h_0)] U_0 dz \quad (2)$$

in which, $P_c (= -\rho g z)$ is the pressure of the current-only field. For waves on a uniform current (Whitham, 1962):

$$Q_{wc} = \overline{\int_{-h}^{\eta} \rho u d z}, M_{wc} = \overline{\int_{-h}^{\eta} (P_{wc} + \rho u^2) d z},$$

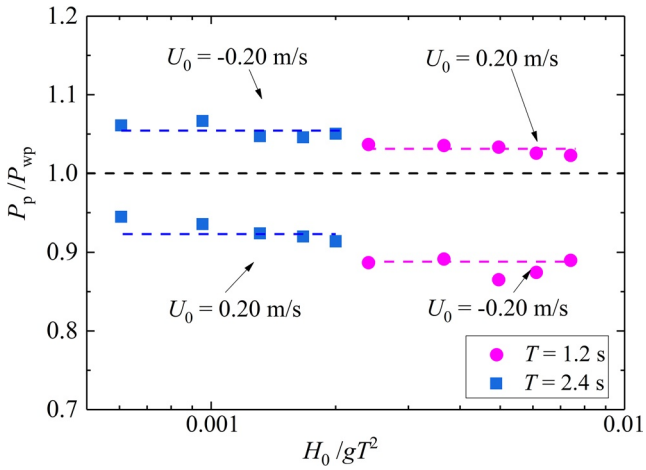

Figure 7. The variation of the peak-to-peak amplitude of mudline pore pressure P_p against the normalized pre-interaction wave height for two typical wave periods with two current velocities ($h_0 = 0.5$ m). The result for wave-only conditions represented by the black dash line ($P_p/P_{wp} = 1$) is included for reference.

$$E_{wc} = \overline{\int_{-h}^{\eta}\left[P_{wc} + \frac{\rho}{2}(u^2 + w^2) + \rho g(z+h)\right]ud\,z} \tag{3}$$

where P_{wc} is the pressure of the wave-current field, u and w are the horizontal and vertical velocity component of the wave-current field, respectively.

Note that the gravitational potential energy terms (the terms contain g) in Equations 1–3 use the seabed bottom as the reference position, which keeps fixed before and after the wave-current interaction (the same treatment can be seen in Whitham, 1962). In addition, due to the continuous operation of the current-generation pump, all the fluid entering the system has a velocity of U_0. Therefore, when considering the momentum and kinetic energy flux conveyed by the superimposed current, the affected mass should be the total mass flux for both the wave and the current. These two issues were ignored in Baddour and Song (1990a, 1990b).

For linear waves, the expressions of u_0, w_0, P_w, u, w, and P_{wc} were summarized in Baddour and Song (1990b). Substituting them into Equations 1–3 and omitting the terms with orders higher than $O(a^2)$, we obtain that in the wave-only field:

$$Q_w = \frac{1}{2}\rho g {a_0}^2 \frac{k_0}{\omega} = \rho h_0 \overline{u_{d0}}$$

$$M_w = \frac{1}{2}\rho g a_0^2\left(\frac{1}{2} + \frac{2k_0h_0}{\sinh 2k_0h_0}\right) + \frac{1}{2}\rho g h_0^2 = S_{x0} + \frac{1}{2}\rho g h_0^2$$

$$E_w = \frac{1}{4}\rho g a_0^2 \frac{\omega}{k_0}\left(1 + \frac{2k_0h_0}{\sinh 2k_0h_0}\right) + \rho g h_0^2 \overline{u_{d0}} = E_0 c_{g0} + \rho g h_0^2 \overline{u_{d0}} \tag{4}$$

where ω is the angular frequency, $\overline{u_{d0}}$ is the relative wave-only drift velocity, $S_{x0} = \frac{1}{2}\rho g a_0^2\left(\frac{1}{2} + \frac{2k_0h_0}{\sinh 2k_0h_0}\right)$ is the radiation stress of the wave-only field (defined by Longuet-Higgins & Stewart, 1960), $E_0 = \frac{1}{2}\rho g {a_0}^2$ is the mean wave-only energy per unit horizontal area, and $c_{g0} = \frac{\omega}{2k_0}\left(1 + \frac{2k_0h_0}{\sinh 2k_0h_0}\right)$ is the group velocity of the wave-only field, that is, the velocity of energy propagation. In the current-only field with depth-uniform velocity:

$$Q_c = \rho h_0 U_0$$

$$M_c = \rho h_0\left(U_0 + \overline{u_{d0}}\right)U_0$$

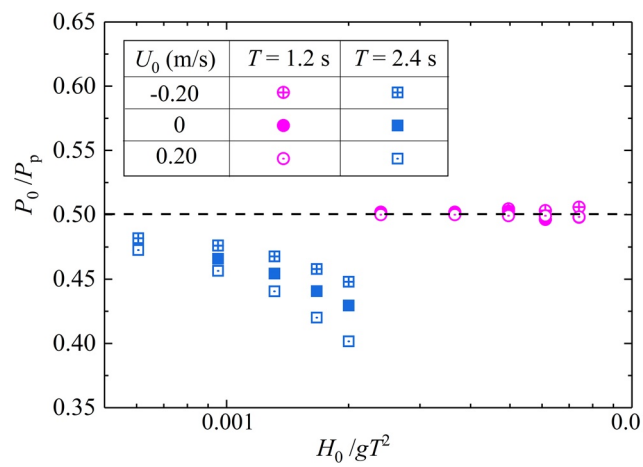

Figure 8. The ratio of pore pressure amplitude under wave trough P_0 to peak-to-peak amplitude P_p versus the normalized pre-interaction wave height for two typical wave periods with different current velocities ($h_0 = 0.5$ m) The black dash line ($P_0/P_p = 0.5$) representing the absolute linear wave, is included for reference.

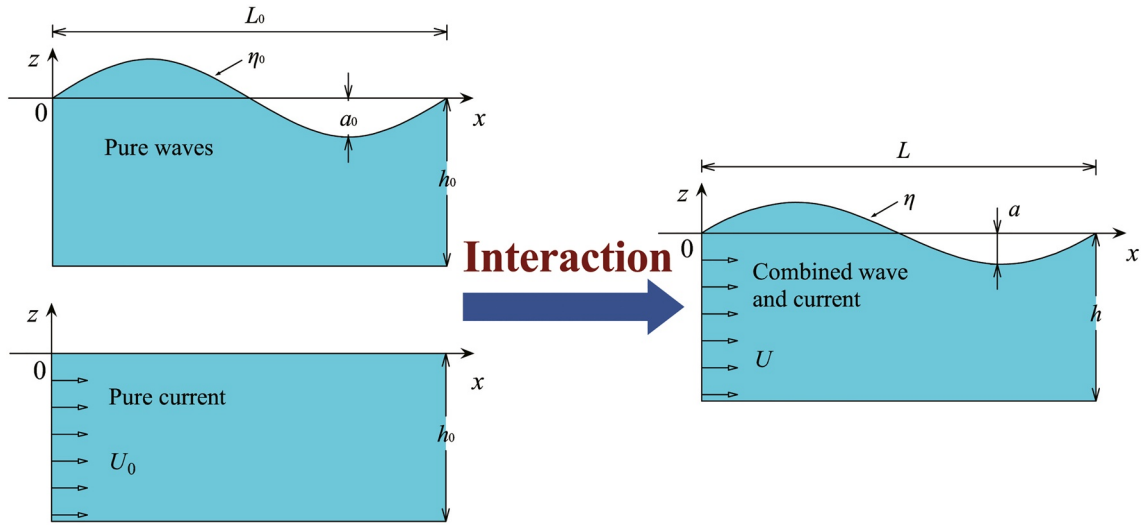

Figure 9. Illustration of wave-current interaction in the present physical modeling. The left side depicts the wave-only and current-only fields before interaction. The right side depicts the combined wave-current field after wave and current interaction.

$$E_c = \frac{1}{2}\rho h_0\left(U_0 + \overline{u_{d0}}\right)U_0^2 + \rho g h_0^2 U_0 \tag{5}$$

For waves on a uniform current:

$$\begin{aligned} Q_{wc} &= \frac{1}{2}\rho a^2 k(c-U)\coth kh + \rho hU = \rho h\left(U + \overline{u_d}\right) \\ M_{wc} &= \frac{1}{2}\rho g a^2\left(\frac{1}{2} + \frac{2kh}{\sinh 2\,kh}\right) + \frac{1}{2}\rho g h^2 + \rho a^2 U k\left(\frac{g}{k}\coth kh\right)^{1/2} + \rho hU^2 = S_x + \frac{1}{2}\rho g h^2 + \rho h\left(U + \overline{u_d}\right)^2 \\ E_{wc} &= \frac{1}{4}\rho g a^2\frac{\omega - kU}{k}\left(1 + \frac{2kh}{\sinh 2\,kh}\right) + \frac{1}{4}\rho g a^2 U\left(3 + \frac{4kh}{\sinh 2\,kh}\right) + \frac{3}{4}\rho g a^2 U^2\left(\frac{k}{\omega - kU}\right) + \frac{\rho}{2}hU^3 \\ &\quad + \rho g h^2\left(U + \overline{u_d}\right) = Ec_{gr} + (E + S_x)U + \frac{1}{2}\rho h\left(U + \overline{u_d}\right)^3 + \rho g h^2\left(U + \overline{u_d}\right) \end{aligned} \tag{6}$$

where the parameters without subscripts in the right terms of Equation 6 indicate those in the wave-current field. $c_{gr} = \frac{\omega - kU}{2k}\left(1 + \frac{2kh}{\sinh 2\,kh}\right)$ is the relative group velocity for the wave-current field. $\left(U + \overline{u_d}\right)$ is the mass transport velocity of the combined wave-current, denoted as U_m hereinafter.

4.2. Solutions of Wave Height and Wavelength

Assuming that the fluid is incompressible and inviscid, the governing equations can be given based on the conservation of mass, momentum, and energy flux (Baddour & Song, 1990b):

$$Q_w + Q_c = Q_{wc} \tag{7}$$

$$M_w + M_c = M_{wc} \tag{8}$$

$$E_w + E_c = E_{wc} \tag{9}$$

Subtract Equation 8 multiplying by U_m from Equation 9, and solve together with Equation 7 by substituting expressions of Equations 4–6. This yields the following equation:

$$E\left(U_0 + c_{gr}\right) - E_0 c_{g0} + S_{x0}U_0 - \frac{1}{2}\rho h U_m(U_0 - U_m)^2 + \frac{1}{2}\rho g U_m(h - h_0)^2 = 0 \tag{10}$$

Since U_m and U of the wave-current field differ from the undisturbed parameters U_0 by terms of $O\left(a^2\right)$, $-\frac{1}{2}\rho h U_m(U_0 - U_m)^2$ is at the order of $O\left(a^4\right)$ and thus can be omitted. The term $\frac{1}{2}\rho g U_m(h - h_0)^2$ can also be omitted due to the insignificant difference between h and h_0 (see Whitham, 1962). Then, Equation 10 turns:

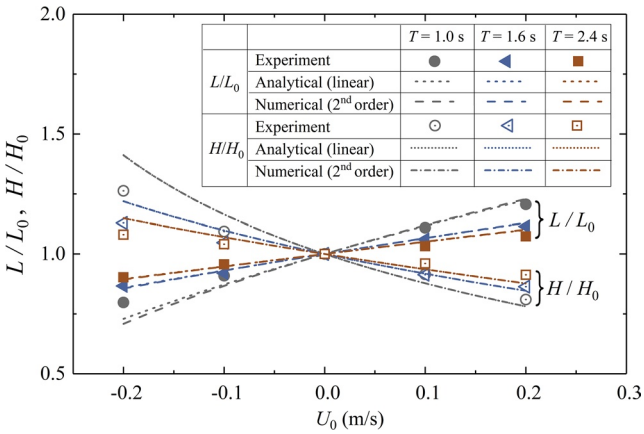

Figure 10. The comparison of wavelength and wave height variation with current velocity between analytical solutions, numerical results, and the experimental data ($h_0 = 0.6$ m). Waves parameters: $T = 1.0$ s, $H_0 = 8.48$ cm (gray); $T = 1.6$ s, $H_0 = 7.62$ cm (blue); $T = 2.4$ s, $H_0 = 9.25$ cm (brown).

$$E\left(U_0 + c_{\mathrm{gr}}\right) - E_0 c_{\mathrm{g}0} + S_{x0} U_0 = 0 \tag{11}$$

where E_0 (or E), S_{x0} are proportional to a_0^2 (or a^2) as aforementioned.

From Equation 11, we further obtain the analytical solution of wave height H in the linear wave-current field:

$$\frac{H}{H_0} = \frac{a}{a_0} = \sqrt{\frac{E}{E_0}} = \sqrt{\frac{2c_0 c_{\mathrm{g}_0} - 4c_{\mathrm{g}_0} U_0 + c_0 U_0}{2c_0\left(c_{\mathrm{gr}} + U_0\right)}} \tag{12}$$

where $c_0 = \frac{\omega}{k_0}$ is the wave-only velocity.

The wavenumber k in the wave-current field can be derived using the dispersion relation:

$$(\omega - kU)^2 = gk \tanh kh \tag{13}$$

Under the linear-wave assumption, U, h in Equation 13 could be replaced by the undisturbed U_0, h_0 to avoid solving the complicated nonlinear equation set composed of Equations 7–9 and 13.

Nevertheless, the explicit analytical solution is not applicable for nonlinear waves due to the presence of higher-order terms. Instead, a numerical scheme needs to be applied instead. For the Stokes 2nd wave and currents, substituting the formulae of u_0, w_0, P_{w}, u, w, and P_{wc} provided in Baddour and Song (1990a) into Equations 1–3 and neglecting terms with higher order than $O\left(a^4\right)$, the expressions of mass, momentum, and energy flux can be obtained, which are extremely complicated and thus omitted here. Using those results and combining the governing Equations 7–9 and 13, the parameters H, k, U, and h in the wave-current field under 2nd order assumption can be solved numerically.

The numerical results (with 2nd order assumption) and analytical solutions (using linear wave assumption) of wavelength $L(= 2\pi/k)$ and wave height H are given in Figure 10, along with the experimental data. As demonstrated in Figure 10, the deviations between the numerical and the analytical results are minor, especially for cases with relatively small wave steepness. This implies that the effects of higher-order terms in wave-current interaction are not significant and the analytical solutions based on the linear wave theory can be utilized for simplicity. Both solutions generally agree well with the experimental data, albeit some deviations can be found for relatively large opposing currents. Similar deviations were also reported by Qi et al. (2019) and attributed to the phenomenon that the wave surface was wrinkled up and approached to break with a large opposing current.

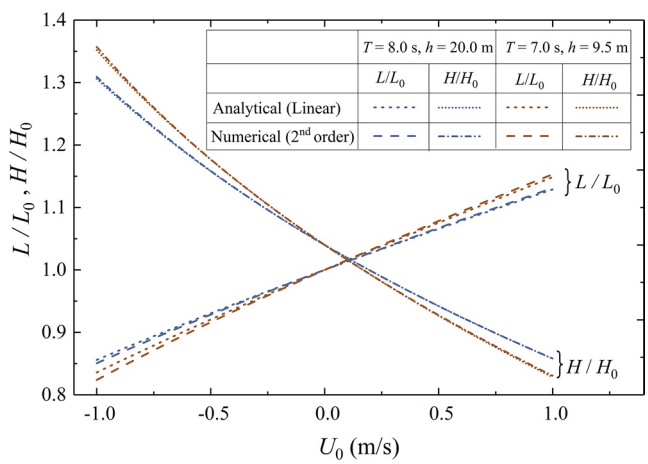

Figure 11. The comparison of wavelength and wave height variation with current velocity between analytical solutions and numerical results for field cases. Wave parameters: $T = 8.0$ s, $H_0 = 3.20$ m, $h_0 = 20.0$ m (blue); $T = 7.0$ s, $H_0 = 2.38$ m, $h_0 = 9.5$ m (brown).

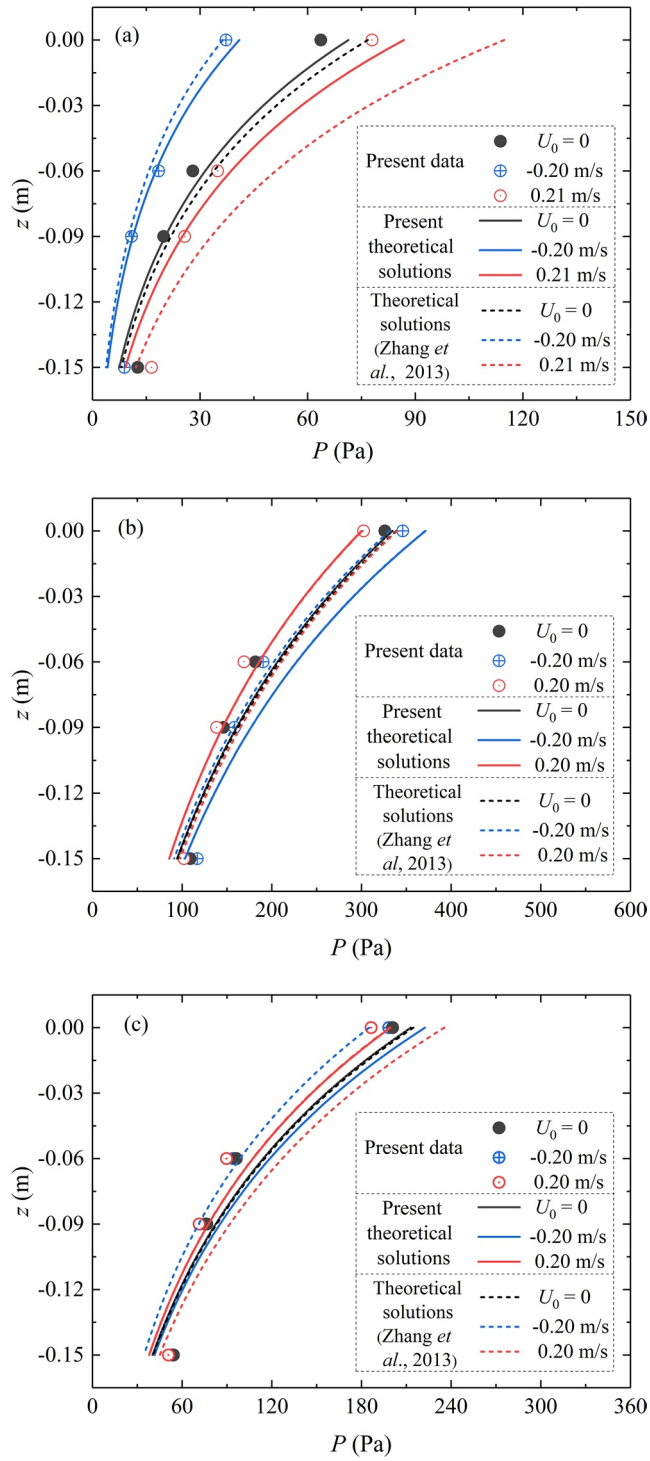

Figure 12. Comparisons of the vertical distributions of the excess pore pressure amplitude along the soil depth between experimental results, present theoretical solutions (Equation 15), and analytical solutions by Zhang et al. (2013): (a) $T = 1.0$ s, $H_0 = 8.47$ cm, $h_0 = 0.6$ m; (b) $T = 2.4$ s, $H_0 = 9.25$ cm, $h_0 = 0.6$ m; (c) $T = 1.6$ s, $H_0 = 7.62$ cm, $h_0 = 0.6$ m.

With wave and current parameters in real ocean conditions (see Esteban et al., 2019; Matutano et al., 2013), the numerical results and analytical solutions of wavelength and wave height are compared in Figure 11. A good agreement can also be observed, which demonstrates that the present explicit solutions are also applicable for field conditions.

Table 2
The Input Parameters for Present Theoretical Predictions

Parameters		Values
Seabed properties	Degree of saturation S_r (%)	99.2
	Coefficient of permeability k_s (m/s)	9.6×10^{-5}
	Shear modulus G (MPa)	10.0
	Porosity of soil n	0.40
	Poisson ratio of soil ν	0.30
Wave parameters	Water depth h (m)	0.6
	Wave height H_0 (cm)	8.47, 7.62, 9.25
	Wave period T (s)	1.0, 1.6, 2.4

4.3. Solution of Pore Pressure Under Combined Wave-Current

Under the loading of combined Stokes 2nd order waves and current, the dynamic pressure (P_b) acting on the seabed can be obtained from water pressure distribution in Baddour and Song (1990b):

$$P_b = P_1 \cos(kx - \omega t) + P_2 \cos 2(kx - \omega t) \tag{14}$$

where $P_1 = \frac{\rho g H}{2 \cosh kh}$, $P_2 = \frac{\rho g k H^2}{8 \sinh 2kh}\left(\frac{3}{\sinh^2 kh} - 1\right)$. The effect of the superimposed current is reflected in the variation of wave number k and wave amplitude H. Substituting the wave characteristics obtained in 4.2, we can derive the dynamic pressure on the seabed surface theoretically.

Taking Equation 14 as the boundary condition at the mudline and based on the quasi-static Biot's consolidation equations (Biot, 1941), the excess pore pressure for a uniform and isotropic seabed can be given as (see Yamamoto et al. (1978) and Zhang et al. (2013) for detailed derivations):

$$p(z) = \sum_{m=1}^{2}\left\{\frac{P_m}{1-2\mu}\left[(1-2\mu-\lambda_m)C_{1m}e^{-mkz} + \frac{\delta_m^2 - m^2k^2}{mk}(1-\mu)C_{2m}e^{-\delta_m z}\right]e^{i m(kx-\omega t)}\right\} \tag{15}$$

where $\lambda_m = \frac{(1-2\mu)n\beta G}{n\beta G+(1-2\mu)}$, $C_{1m} = \frac{\delta_m - \delta_m\mu + mk\mu}{\delta_m - \delta_m\mu + mk\mu + mk\lambda_m}$, $C_{2m} = \frac{mk\lambda_m}{(\delta_m - mk)(\delta_m - \delta_m\mu + mk\mu + mk\lambda_m)}$, $\delta_m^2 = m^2k^2 - \frac{i m\omega\gamma_w}{k_s}\left(n\beta + \frac{1-2\mu}{2G(1-\mu)}\right)$, and β is the compressibility of pore fluid.

As aforementioned, Zhang et al. (2013) also proposed an analytical solution for pore pressure response in the seabed under combined Stokes 3rd order wave and a uniform current. The solution in Zhang et al. (2013) has a similar form to that in the present work but neglected the wave height variation. The wave conditions in the present experiments are mainly in the range of Stokes 2nd or 3rd order wave (according to Le Méhauté, 1976). Therefore, both the solution of Zhang et al. (2013) and the present one (Equation 15) are considered to be appropriate. Figure 12 shows the comparison of the vertical distributions of the excess pore pressure amplitudes P along the soil depth from experimental measurement, present theoretical solutions (Equation 15), and analytical solutions by Zhang et al. (2013). The input parameters for the theoretical predictions are given in Table 2, in which the saturation degree S_r is considered a key influencing factor for defining the pore pressure distribution (Okusa, 1985; Qi & Gao, 2018). Nevertheless, the saturation degree is difficult to measure accurately (Michallet et al., 2009). In the

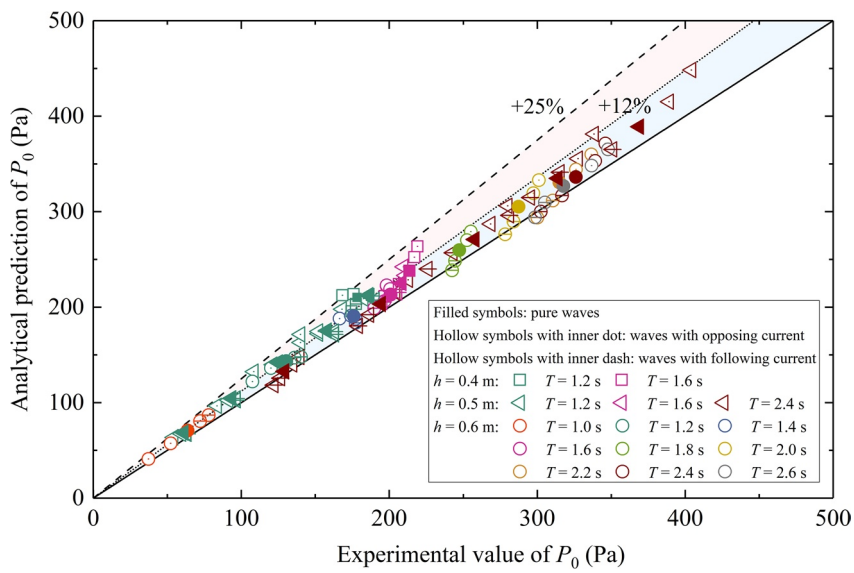

Figure 13. The comparison between theoretical solutions and experimental data of mudline pore pressure amplitudes, with all the test cases in Table 1 included. Filled symbols represent wave-only conditions, while open symbols with an inner dot are opposing current, and with an inner dash are following current.

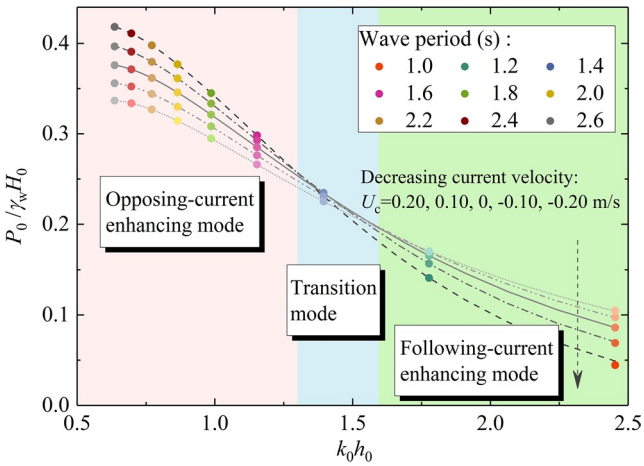

Figure 14. The theoretical variation of the seabed surface pore pressure with the superimposed current for experimental cases ($H_0 = 8.50$ cm, $h_0 = 0.6$ m), predicted by Equation 16. Symbols and lines from light to dark within each color represent the current velocity decreasing from 0.2 to −0.2 m/s.

present comparison, the value of S_r is calibrated by fitting the experimental data for wave-only conditions. Note that the dynamic pressure response at the mudline is only related to the wave parameters (see Equation 14), and would not be affected by the calibrated value of the saturation degree.

As shown in Figure 12a for cases with $T = 1.0$ s, the predictions of pore pressure distribution from both the present theory and the solution by Zhang et al. (2013) generally agree with the experimental results. However, the deviations of the present results from the experimental data are remarkably smaller. Note that the slight difference between two analytical solutions for the wave-only condition originates from different wave assumptions (i.e., second and third order). Figure 12b demonstrates the comparisons for cases of $T = 2.4$ s, in which the influence of the superimposed current seems to be insignificant when predicted by Zhang et al. (2013). In contrast, the present solution indicates an enhancing effect of the opposing current and a reducing effect of the following current, which agrees well with the experimental data. For cases of $T = 1.6$ s shown in Figure 12c, the solution by Zhang et al. (2013) implies a following-current enhancing mode, but the present solution shows that the following current would reduce the pore pressure and the opposing current has an inappreciable effect, which again agrees better with the experimental data. The relatively larger deviations of the solution by Zhang et al. (2013) should be attributed to ignoring the current-induced variation of wave height.

5. Parametric Analyses for Dynamic Mudline Pore Pressure

To further predict the effect of the superimposed current on the dynamic pore pressure response with our analytical model, a comparison of the mudline pore pressure is performed to validate our theoretical solutions against experimental results. Based on Equation 14, the amplitude of combined wave-current induced mudline pore pressure under the wave trough (P_0) can be obtained by:

$$P_0 = |(P_b)_{\min}| = -P_b|_{kx-\omega t=\pi} = \frac{\rho g H}{2\cosh kh} - \frac{\rho g k H^2}{8\sinh 2kh}\left(\frac{3}{\sinh^2 kh} - 1\right) \tag{16}$$

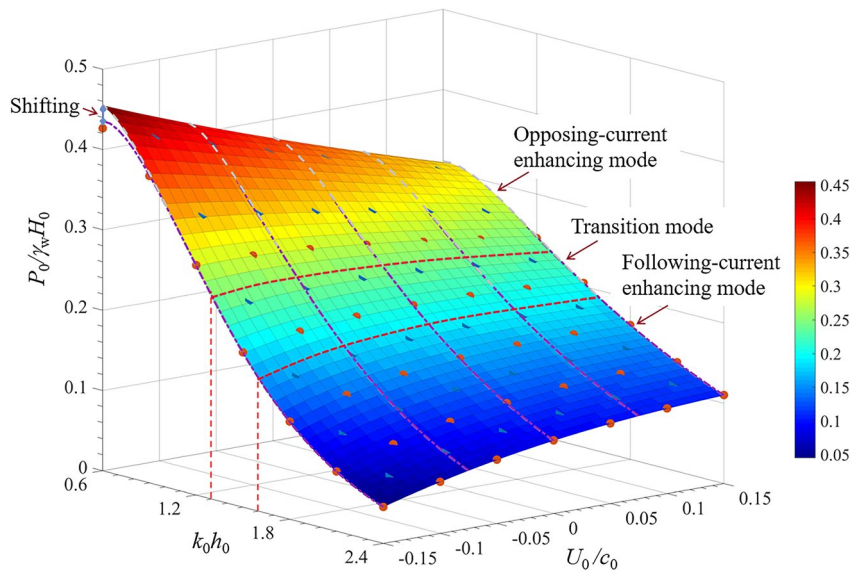

Figure 15. Theoretical predictions of the mudline pore pressure amplitude $P_0/\gamma_w H_0$ with k_0h_0 and U_0/c_0. The backbone surface represents cases in lab conditions with $H_0 = 8.50$ cm, $h_0 = 0.6$ m. Gray dash lines represent cases in lab conditions with $H_0 = 5.50$ cm, $h_0 = 0.4$ m. Purple dash-dot lines represent cases in lab conditions with $H_0 = 8.50$ cm, $h_0 = 0.4$ m. Red circles represent field conditions with $H_0 = 2.35$ m, $h_0 = 9.5$ m. Blue triangles represent field conditions with $H_0 = 3.20$ m, $h_0 = 20.0$ m. Two red dash lines on the backbone surface represent the range of the transition mode.

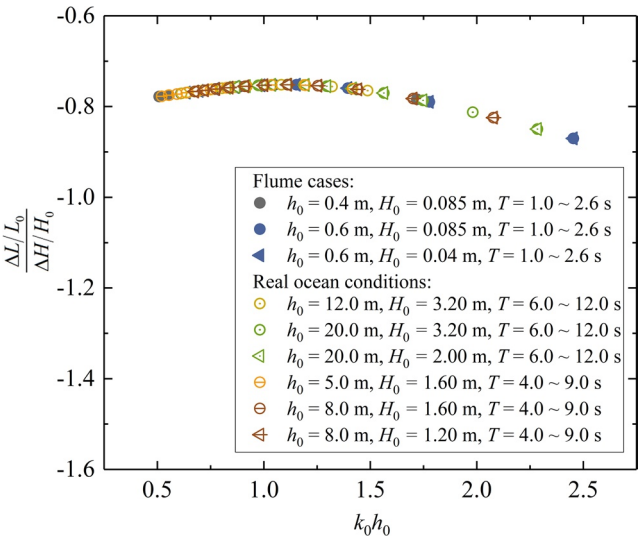

Figure 16. The ratio of relative wavelength variation to relative wave height alteration $\frac{\Delta L/L_0}{\Delta H/H_0}$ induced by the current under a wide range of wave conditions. For flume cases, the interval between periods is 0.2 s; for real ocean situations, the wave period interval is 0.5 s.

Substituting the parameters of pre-interaction wave and current in the present experiments (see Table 1) into Equation 16, the theoretical predictions of mudline pore pressure amplitude are obtained; then compared with the experimental data in Figure 13. A good agreement can be observed between the theoretical results and experimental data, with the maximum deviation of no more than 25%. As indicated by the filled symbols, theoretical predictions for the mudline pore pressure amplitude induced by the wave-only loading without the current effect are inherently larger than experimental data, which may be because of the neglection of the rough and permeable seabed of the experiment, which can dissipate wave energy. This also leads to slightly larger theoretical predictions under combined wave-current loading. In addition, Figure 13 demonstrates that most predictions fall within the 12% error bar. It can be observed that the predictions with a larger deviation of 12% ~ 25% generally correspond to cases with relatively large wave steepness and shallow water depth involving significant nonlinearity, for which the present analytical solution may have limited accuracy.

Using our analytical model, the three variation models of P_0 under superimposed currents are predicted in Figure 14, in comparison to Figure 4 with experimental data. Afore-identified three typical variation modes, including following-current enhancing mode, transition mode, and opposing-current enhancing mode, are clearly presented and are generally consistent with experimental observations. A minor shift of the range for the transition mode is observed with the analytical solution, that is, from $1.1 < k_0h_0 < 1.4$ to $1.3 < k_0h_0 < 1.6$, compared to the experimental results. Such deviation may be due to ideal assumptions in the theoretical derivation: (a) the current velocity is uniformly distributed along the depth; and (b) there is no energy dissipation before and after the wave-current interaction. For the wave height and wavelength variations induced by the wave-current coupling effect, ideal assumptions could lead to deviations between theoretical solutions and experimental results (see Figure 10), which may further induce the shift of the present transition mode. Note that the exact reason for the shift of the transition mode still needs further investigation.

The applicability of the three modes and their ranges for the predictions in real sea conditions (characterized by k_0h_0 and normalized current velocity U_0/c_0) is further verified in Figure 15. The results among all the examined cases with various wave and current parameters for both laboratory and field conditions (Esteban et al., 2019; Matutano et al., 2013) exhibit a good consistency with our analysis. This confirms that the variation mode of $P_0/\gamma_w H_0$ with superimposed U_0/c_0 can be generally determined by the parameter k_0h_0. Based on the analytical solution, the range of $1.3 < k_0h_0 < 1.6$ can be considered as a general criterion for transition between following-current enhancing mode and opposing-current enhancing mode. Note that the different wave height does not affect the variation modes, albeit a relatively large wave height containing pronounced nonlinearity would induce shifting of $P_0/\gamma_w H_0$, especially for small k_0h_0 (see Figure 15).

Finally, let us explore the physical mechanism in the three variation modes. An analysis is carried out based on Equation 16. For simplification, we will focus on the linear principal term of the mudline pore pressure, that is, the first term in Equation 16, which mainly determines the mudline pore pressure. As we know, a superimposed current will induce opposite effects on the wavelength and the wave height, that is, a following/opposing current will increase/decrease wavelength and decrease/increase wave height. Therefore, the variation of pore pressure with superimposed current depends on the combined effect of wavelength and wave height change. The Taylor expansion of the linear term for P_0 near (H_0, L_0) is:

$$P_0(H_0+\Delta H, L_0+\Delta L) - P_0(H_0, L_0) \approx \Delta H \frac{\partial P_0}{\partial H}\Big|_{H=H_0, L=L_0} + \Delta L \frac{\partial P_0}{\partial L}\Big|_{H=H_0, L=L_0}$$
$$\approx \Delta H \frac{\rho g}{2\cosh\left(\frac{2\pi}{L_0}h_0\right)} + \Delta L \frac{\rho g H_0 \sinh\left(\frac{2\pi}{L_0}h_0\right)}{2\cosh^2\left(\frac{2\pi}{L_0}h_0\right)} \frac{2\pi h_0}{L_0^2} \quad (17)$$

where the first term on the right-hand side reveals the effect of wave height changes on the pore pressure, and the second term represents the influence on the pore pressure induced by the wavelength alteration. The ratio of the latter to the former is:

$$\frac{\Delta L \frac{\rho g H_0 \sinh\left(\frac{2\pi}{L_0}h_0\right)}{2\cosh^2\left(\frac{2\pi}{L_0}h_0\right)} \frac{2\pi h_0}{L_0^2}}{\Delta H \frac{\rho g}{2\cosh\left(\frac{2\pi}{L_0}h_0\right)}} = \frac{\Delta L/L_0}{\Delta H/H_0} \tanh(k_0 h_0) k_0 h_0 \tag{18}$$

in which $\Delta H/H_0$ and $\Delta L/L_0$ are the relative change of wave height and wavelength induced by the superimposed current, respectively.

Figure 16 gives the values of $\frac{\Delta L/L_0}{\Delta H/H_0}$ under different wave conditions, including flume cases and real ocean conditions. To satisfy the constraints of the Taylor expansion, the superimposed current velocities are small: 0.001 m/s for flume conditions and 0.005 m/s for real ocean situations. It can be seen that for a wide range of wave conditions, the variation of $\frac{\Delta L/L_0}{\Delta H/H_0}$ with k_0h_0 almost overlaps into a uniform curve. The values of $\frac{\Delta L/L_0}{\Delta H/H_0}$ generally fall into $-0.75 \sim -0.90$ (the negative sign implies that the current has opposite effects on the wavelength and wave height). The same conclusion about $\frac{\Delta L/L_0}{\Delta H/H_0}$ can also be obtained from the experimental data (see Figure 10). Therefore, Equation 18 indicates that the relative water depth for the wave-only field k_0h_0 is a key dimensionless parameter to determine whether the effect of wavelength or wave height change dominates.

For a relatively large k_0h_0 ($k_0h_0 > 1.6$), $\tanh(k_0h_0) \to 1$ and the absolute value of Equation 18 is larger than 1. Under such circumstances, the change of the wavelength has more effect on the pore pressure than wave height. The following current amplifies the wavelength; thus increases the pore pressure. Thereby, with relatively large k_0h_0, we observed the following-current enhancing mode. In contrast, for a relatively small k_0h_0 ($k_0h_0 < 1.3$), $\tanh(k_0h_0) < 1$ and the absolute value of Equation 18 is clearly less than 1, which implies the predominant effect of wave height change on pore pressure. Therefore, the opposing current induced increase of the wave height can amplify the pore pressure in the sandy bed. When k_0h_0 falls into the intermediate range, the absolute value of Equation 18 is near 1, indicating that the two opposite effects of wavelength and wave height variation under superimposed currents are nearly neutralized. This would lead to an insignificant influence on the pore pressure, corresponding to the observed transition mode.

The above analysis can well explain the present experimental results in Figures 4, 5, and 7. It is worthwhile to mention that only the linear principal term is considered in the above analysis. When the wave nonlinearity is significant, the second term in Equation 16 (i.e., the nonlinear term) cannot be ignored in the analysis. This nonlinear term will lead to the asymmetry between wave crest and trough, and further enhance the current effect on P_0, as revealed in Section 3.3 (Figure 6, $T = 2.4$ s). Nevertheless, since the nonlinear term is usually smaller than the linear term for intermediate water depth, the variation mode of P_0 with current can be generally determined by k_0h_0.

6. Conclusions

This study has gained an insightful view of the combined wave-current induced pore pressure response within a non-cohesive seabed. A series of experimental tests spanning a wide range of wave periods, water depths, and wave heights have been carried out to reveal the effect of a following/opposing current on the excess pore pressure response in the sandy bed. Novel analytical solutions have also been derived in this work. First, an explicit analytical solution of wave height in the linear wave-current field has been derived, which has been compared and validated against the numerical results under combined Stokes 2nd order waves and currents, and the measured wave height in the flume tests. With this updated wave height, an analytical solution for the combined wave-current induced pore pressure response has been further provided and validated with the experimental measurement. The following conclusions can be drawn based on the experimental observations and theoretical analyses:

1. Three typical variation modes regarding the influence of the current on the wave-induced pore pressure have been identified in the intermediate water depth. Besides the following-current enhancing mode, which had been substantially verified by previous experiments and theoretical solutions, another two new variation modes, that is, transition mode and opposing-current enhancing mode, have been newly identified. The

following/opposing-current enhancing mode depicts that a following/opposing-directional current to waves can enhance the pore pressure amplitude.

2. The variation mode is found to be dependent on the relative water depth k_0h_0, where k_0, h_0 are the wavenumber and water depth in wave-only conditions, respectively. For the present experiments, the range of $k_0h_0 > 1.4$, $1.1 < k_0h_0 < 1.4$, and $k_0h_0 < 1.1$ can be approximately categorized as the following-current enhancing mode, transition mode, and opposing-current enhancing mode, respectively. The wave height does not affect the range of the variation mode, albeit a large wave height would potentially enhance the current effect on pore pressure amplitudes under the wave trough.
3. The predictions from the proposed analytical model generally coincide with the experimental results. The analytical solution is capable of reflecting the three typical variation modes of the normalized mudline pore pressure amplitude under combined waves and currents. The range of the transition mode determined by the analytical solution reasonably agrees with the experimental results with minor deviations due to simplification. For all the examined cases spanning a wide range of wave and current parameters, the theoretical diagram is applicable to predict the current effect on the wave-induced mudline pore pressure amplitude, for both laboratory and field conditions.
4. The superimposed current has opposite effects on wavelength and wave height. that is, a following/opposing current can increase/decrease wavelength while decrease/increase wave height. Thus the variation mode of pore pressure with current can be explained by the combined influence of wavelength and wave height. For a relatively large k_0h_0 ($k_0h_0 > 1.4$ in the present experiment), the change of wavelength has a more significant effect on the pore pressure, leading to the following-current enhancing mode; for a relatively small k_0h_0 ($k_0h_0 < 1.1$ in the present experiment), the change of wave height has the predominant effect, causing the opposing-current enhancing mode; when k_0h_0 falls into the intermediate range, the effects of wavelength and wave height variation on the pore pressure are nearly neutralized, corresponding the transition mode.

Nomenclature

a	wave amplitude after wave-current interaction
a_0	wave-only amplitude
c_0	wave-only velocity
c_{g0}	group velocity of the wave-only field
c_g	group velocity of the combined wave-current field
c_{gr}	relative group velocity of the combined wave-current field
E_0	mean wave-only energy density per unit horizontal area
E	mean wave-current energy density per unit horizontal area
E_c	mean energy flux of the current-only field
E_w	mean energy flux of the wave-only field
E_{wc}	mean energy flux of the combined wave-current field
h_0	water depth of the wave-only and current-only field
h	water depth after wave-current interaction
H_0	wave height of the wave-only field
H	wave height of the combined wave-current field
k_0	wave-only number
k	wave number in the wave-current field
L_0	wavelength of the wave-only field
L	wavelength of the combined wave-current field
M_c	mean momentum flux of the current-only field
M_w	mean momentum flux of the wave-only field
M_{wc}	mean momentum flux of the combined wave-current field
p	excess pore pressure
P	excess pore pressure amplitude
P_0	mudline pore pressure amplitude
P_b	dynamic pressure acting on the seabed surface
P_c	pressure of the current-only field
P_p	peak-to-peak amplitude of mudline pore pressure

P_{wp}	peak-to-peak amplitude of mudline pore pressure for wave-only
P_w	pressure of the wave-only field
P_{w0}	mudline pore pressure amplitude for the wave-only field
P_{wc}	pressure of the wave-current field
Q_c	mean mass flux of the current-only field
Q_w	mean mass flux of the wave-only field
Q_{wc}	mean mass flux of the combined wave-current field
S_{x0}	radiation stress of the wave-only field
S_x	radiation stress of the wave-current field
T	wave period
u_0	horizontal velocity components of the wave-only field
u	particle horizontal velocity of the wave-current field
$\overline{u_{d0}}$	relative wave-only drift velocity
$\overline{u_d}$	relative wave-current drift velocity
U	average velocity of the wave-current field
U_c	measured current velocity at the level of 0.15 m
U_m	mass transport velocity of the combined wave-current field
U_0	velocity of the superimposed uniform current
w_0	vertical velocity components of the wave-only field
w	vertical velocity components of the wave-current field
η_0	wave-only surface elevation
η	wave-current surface elevation
ρ	fluid density
ω	angular frequency

Data Availability Statement

Data collected during the flume experiment are available at Yang et al. (2022).

Acknowledgments
The authors would like to thank the National Natural Science Foundation of China (Grants. 11825205 and 11972036) and the Youth Innovation Promotion Association CAS (Grant 2021018) for financial support.

References

Anderson, D., Cox, D., Mieras, R., Puleo, J. A., & Hsu, T. J. (2017). Observations of wave-induced pore pressure gradients and bed level response on a surf zone sandbar. *Journal of Geophysical Research: Oceans*, *122*(6), 5169–5193. https://doi.org/10.1002/2016jc012557

Baddour, R. E., & Song, S. (1990a). Interaction of higher-order water waves with uniform currents. *Ocean Engineering*, *17*(6), 551–568. https://doi.org/10.1016/00298018(90)-90023-Y

Baddour, R. E., & Song, S. (1990b). On the interaction between waves and currents. *Ocean Engineering*, *17*(1–2), 1–21. https://doi.org/10.1016/0029-8018(90)90011-T

Bear, J. (1972). *Dynamics of fluids in porous media*. Courier Corporation.

Biot, M. A. (1941). General theory of three-dimensional consolidation. *Journal of Applied Physics*, *12*(2), 155–164. https://doi.org/10.1063/1.1712886

Brevik, I., & Bjørn, A. (1979). Flume experiment on waves and currents. I. Rippled bed. *Coastal Engineering*, *3*, 149–177. https://doi.org/10.1016/0378-3839(79)90019-X

Chang, K. T., & Jeng, D. S. (2014). Numerical study for wave-induced seabed response around offshore wind turbine foundation in Donghai offshore wind farm, Shanghai, China. *Ocean Engineering*, *85*, 32–43. https://doi.org/10.1016/j.oceaneng.2014.04.020

Chowdhury, B., Dasari, G. R., & Nogami, T. (2006). Laboratory study of liquefaction due to wave–seabed interaction. *Journal of Geotechnical and Geoenvironmental Engineering*, *132*(7), 842–851. https://doi.org/10.1061/(ASCE)10900241(2006)-132:7(842)

Cuéllar, P., Baeßler, M., & Rücker, W. (2012). Pore pressure accumulation and soil softening around pile foundations for offshore wind turbines. *ASME 2012 International Conference on Ocean, Offshore and Arctic Engineering*, 219–228. https://doi.org/10.1115/OMAE2012-84201

De Groot, M. B., Kudella, M., Meijers, P., & Oumeraci, H. (2006). Liquefaction phenomena underneath marine gravity structures subjected to wave loads. *Journal of Waterway, Port, Coastal, and Ocean Engineering*, *132*(4), 325–335. https://doi.org/10.1061/(ASCE)0733-950X(2006)132:4(325)

El-Shahat, S. A., Li, G., & Fu, L. (2021). Investigation of wave–current interaction for a tidal current turbine. *Energy*, *227*, 120377. https://doi.org/10.1016/j.energy.2021.120377

Esteban, M. D., López-Gutiérrez, J. S., Negro, V., & Sanz, L. (2019). Riprap scour protection for monopiles in offshore wind farms. *Journal of Marine Science and Engineering*, *7*(12), 440. https://doi.org/10.3390/jmse7120440

Hsu, H. C., Chen, Y. Y., Hsu, J. R., & Tseng, W. J. (2009). Nonlinear water waves on uniform current in Lagrangian coordinates. *Journal of Nonlinear Mathematical Physics*, *16*(01), 47–61. https://doi.org/10.1142/S1402925109000054

Jeng, D. S. (2018). *Mechanics of Wave-seabed-structure interactions: Modelling, processes and applications*. Cambridge University Press.

Klammler, H., Penko, A. M., Staples, T., Sheremet, A., & Calantoni, J. (2021). Observations and modeling of wave-induced burial and sediment entrainment: Likely importance of degree of liquefaction. *Journal of Geophysical Research: Oceans*, *126*(8), e2021JC017378. https://doi.org/10.1029/2021JC017378

Le Méhauté, B. (1976). *An introduction to hydrodynamics and water waves*. Springer.

Li, Y., Ong, M. C., Fuhrman, D. R., & Larsen, B. E. (2020). Numerical investigation of wave-plus-current induced scour beneath two submarine pipelines in tandem. *Coastal Engineering*, *156*, 103619. https://doi.org/10.1016/j.coastaleng.2019.103619

Li, Y., Ong, M. C., & Tang, T. (2020). A numerical toolbox for wave-induced seabed response analysis around marine structures in the OpenFOAM® framework. *Ocean Engineering*, *195*, 106678. https://doi.org/10.1016/j.oceaneng.2019.106678

Liao, C. C., Jeng, D. S., & Zhang, L. L. (2015). An analytical approximation for dynamic soil response of a porous seabed due to combined wave and current loading. *Journal of Coastal Research*, *31*(5), 1120–1128. https://doi.org/10.1016/j.oceaneng.2012.09.001

Lin, Z., Guo, Y., Jeng, D. S., Liao, C., & Rey, N. (2016). An integrated numerical model for wave–soil–pipeline interactions. *Coastal Engineering*, *108*, 25–35. https://doi.org/10.1016/j.coastaleng.2015.11.003

Liu, B., Jeng, D. S., & Zhang, J. S. (2014). Dynamic response in a porous seabed of finite depth to combined wave and current loadings. *Journal of Coastal Research*, *30*(4), 765–776. https://doi.org/10.2112/JCOASTRES-D-12-00064.1

Longuet-Higgins, M. S., & Stewart, R. (1960). Changes in the form of short gravity waves on long waves and tidal currents. *Journal of Fluid Mechanics*, *8*(4), 565–583. https://doi.org/10.1017/S0022112060000803

Longuet-Higgins, M. S., & Stewart, R. (1961). The changes in amplitude of short gravity waves on steady non-uniform currents. *Journal of Fluid Mechanics*, *10*(4), 529–549. https://doi.org/10.1017/S0022112061000342

Madsen, O. S. (1978). Wave-induced pore pressures and effective stresses in a porous bed. *Géotechnique*, *28*(4), 377–393. https://doi.org/10.1680/geot.1978.28.4.377

Matutano, C., Negro, V., López-Gutiérrez, J. S., & Esteban, M. D. (2013). Scour prediction and scour protections in offshore wind farms. *Renewable Energy*, *57*, 358–365. https://doi.org/10.1016/j.renene.2013.01.048

Michallet, H., Mory, M., & Piedra-Cueva, I. (2009). Wave-induced pore pressure measurements near a coastal structure. *Journal of Geophysical Research*, *114*(C6), C06019. https://doi.org/10.1029/2008JC005071

Okusa, S. (1985). Wave-induced stresses in unsaturated submarine sediments. *Géotechnique*, *35*(4), 517–532. https://doi.org/10.1680/geot.1985.35.4.517

Oumeraci, H. (1994). Review and analysis of vertical breakwater failures—Lessons learned. *Coastal Engineering*, *22*(1–2), 3–29. https://doi.org/10.1016/03783839(94)9004-69

Peregrine, D. H. (1976). Interaction of water waves and currents. *Advances in Applied Mechanics*, *16*, 9–117. https://doi.org/10.1016/S0065-2156(08)70087-5

Qi, W. G., & Gao, F. P. (2014). Physical modeling of local scour development around a large-diameter monopile in combined waves and current. *Coastal Engineering*, *83*, 72–81. https://doi.org/10.1016/j.coastaleng.2013.10.007

Qi, W. G., & Gao, F. P. (2018). Wave induced instantaneously-liquefied soil depth in a non-cohesive seabed. *Ocean Engineering*, *153*, 412–423. https://doi.org/10.1016/j.oceaneng.2018.01.107

Qi, W. G., Li, C. F., Jeng, D. S., Gao, F. P., & Liang, Z. (2019). Combined wave-current induced excess pore pressure in a sandy seabed: Flume observations and comparisons with theoretical models. *Coastal Engineering*, *147*, 89–98. https://doi.org/10.1016/j.coastaleng.2019.02.006

Qi, W. G., Liu, J., Gao, F. P., Li, B., & Chen, Q. G. (2022). Quantifying the spatiotemporal evolution of the turbulent horseshoe vortex in front of a vertical cylinder. *Physics of Fluids*, *34*(1), 015110. https://doi.org/10.1063/5.0076648

Sui, T., Zhang, C., Guo, Y., Zheng, J., Jeng, D., Zhang, J., & Zhang, W. (2016). Three-dimensional numerical model for wave-induced seabed response around monopile. *Ships and Offshore Structures*, *11*(6), 667–678. https://doi.org/10.1080/17445302.2015.1051-312

Thomas, G. (1981). Wave-current interactions: An experimental and numerical study. Part 1. Linear waves. *Journal of Fluid Mechanics*, *110*, 457–474. https://doi.org/10.1017/S0022112081000839

Whitham, G. B. (1962). Mass, momentum and energy flux in water waves. *Journal of Fluid Mechanic*s, *12*(1), 135–147. https://doi.org/10.1017/S0022112062000099

Whitham, G. B. (1999). *Linear and nonlinear waves*. John Wiley & Sons.

Yamamoto, T., Koning, H. L., Sellmeijer, H., & Van Hijum, E. P. (1978). On the response of a poro-elastic bed to water waves. *Journal of Fluid Mechanics*, *87*(1), 193–206. https://doi.org/10.1017/S0022112078003006

Yang, L. J., Qi, W. G., Li, Y. Z., & Gao, F. P. (2022). Wave-current coupling effects on the variation modes of pore pressure response in a sandy seabed: Physical modeling and explicit approximations [Dataset]. Zenodo. https://doi.org/10.5281/zenodo.6969773

Ye, J. H., & Jeng, D. S. (2012). Response of porous seabed to nature loadings: Waves and currents. *Journal of Engineering Mechanics*, *138*(6), 601–613. https://doi.org/10.1061/(ASCE)EM.1943-7889.0000356

Zen, K., & Yamazaki, H. (1991). Field observation and analysis of wave-induced liquefaction in seabed. *Soils and Foundations*, *31*(4), 161–179. https://doi.org/10.3208/sandf1972.31.4_161

Zhang, J., Li, Q., Ding, C., Zheng, J., & Zhang, T. (2016). Experimental investigation of wave-driven pore-water pressure and wave attenuation in a sandy seabed. *Advances in Mechanical Engineering*, *8*(6), 1–10. https://doi.org/10.1177/1687814016651207

Zhang, X., Simons, R., Zheng, J., & Zhang, C. (2021). A review of the state of research on wave-current interaction in nearshore areas. *Ocean Engineering*, *243*, 110202. https://doi.org/10.1016/j.oceaneng.2021.110202

Zhang, Y., Jeng, D. S., Gao, F. P., & Zhang, J. S. (2013). An analytical solution for response of a porous seabed to combined wave and current loading. *Ocean Engineering*, *57*, 240–247. https://doi.org/10.1016/j.oceaneng.2012.09.001

Zhou, M. Z., Liu, H., Jeng, D. S., Qi, W. G., & Fang, Q. (2021). Modelling the wave-induced instantaneous liquefaction in a non-cohesive seabed as a nonlinear complementarity problem. *Computers and Geotechnics*, *137*, 104275. https://doi.org/10.1016/j.compgeo.2021.104275

Zhou, M. Z., Qi, W. G., Jeng, D. S., & Gao, F. P. (2021). A non-Darcy flow model for a non-cohesive seabed involving wave-induced instantaneous liquefaction. *Ocean Engineering*, *239*, 109807. https://doi.org/10.1016/j.oceaneng.2021.109807